Convective Drying of Films of Polymer Solutions: Front Propagation Revealed by Thermal Measurements

Apolline Faidherbe, Emmanuel Garre, Maxence Wilmet, Jérémie Teisseire, François Lequeux, Laurence Talini

▶ **To cite this version:**

Apolline Faidherbe, Emmanuel Garre, Maxence Wilmet, Jérémie Teisseire, François Lequeux, et al.. Convective Drying of Films of Polymer Solutions: Front Propagation Revealed by Thermal Measurements. Langmuir, 2024, 10.1021/acs.langmuir.4c02617 . hal-04689085

HAL Id: hal-04689085
https://hal.science/hal-04689085v1

Submitted on 5 Sep 2024

HAL is a multi-disciplinary open access archive for the deposit and dissemination of scientific research documents, whether they are published or not. The documents may come from teaching and research institutions in France or abroad, or from public or private research centers.

L'archive ouverte pluridisciplinaire **HAL**, est destinée au dépôt et à la diffusion de documents scientifiques de niveau recherche, publiés ou non, émanant des établissements d'enseignement et de recherche français ou étrangers, des laboratoires publics ou privés.

Convective drying of films of polymer solutions: Front propagation revealed by thermal measurements

5 septembre 2024

Apolline Faidherbe[1], Emmanuel Garre[1], Maxence Wilmet[2], Jérémie Teisseire[2], François Lequeux[3] and Laurence Talini[1*]

1. CNRS, Surface du Verre et Interfaces, Saint-Gobain, 93300 Aubervilliers, France.
2. Saint-Gobain Resarch Paris, 93300 Aubervilliers, France.
3. CNRS Sciences et Ingénierie de la Matière Molle, ESPCI Paris, PSL Research University, Sorbonne Université 75005 Paris, France.
*corresponding author : laurence.talini@cnrs.fr

Abstract : We report on the drying of films of polymer solutions under a controlled laminar air flow. Temperature measurements reveal that a drying front propagates in the film at constant velocity. Using thermal calibration, we are able to quantitatively determine the local drying rate of the film, and we find it agrees with conservation arguments. We further show that a simple mass balance allows us to relate the front velocity to the drying rate.

1 Introduction

Evaporation of water is a slow process because, in usual conditions, it is limited by diffusion of vapor in the atmosphere. Techniques to accelerate drying have been developed in industrial lines. Submitting the sample from which water or solvent must be extracted to a gas flow is particularly efficient and convective drying is widely used, for instance in the food [13] and coating [8] industries. When a thin liquid film is dried in a gas flow, as in a coating process, a front forms at the upstream edge, which propagates and separates a dry region from a liquid one. During the so-called directional drying, the microscopic structure of the sample may be modified by the passage of the front ; for instance, ordering [6] or aggregation [12] have been reported in colloidal suspensions.

The kinetics of the front in unidirectional drying has been the object of less attention, although it could provide crucial information on the local drying rate. Measurements of global drying kinetics by techniques such as gravimetry [2], were conducted but they do not provide information on the front propagation. Recently, the volume fraction distribution of drying colloidal suspensions obtained from transmitted light intensity in presence of and added dye [9] was reported but the authors did not discuss the front kinetics. Other systems dried in air flows were studied with spatially resolved techniques, such as Fourier Transform Infrared Microscopy [19] or thickness measurements based on laser reflectometry [20, 21], but the front velocity was not inferred from those measurements, although the effect of the front passage on local shrinking was emphasised.

In contrast, the kinetics of spontaneously forming drying fronts in evaporating films has been considered in several studies. Without air convection, lateral fronts form because drying is faster at the edges of the film. In the literature, the mechanism of faster drying is under debate and is attributed either to a larger evaporation flux at the edges [3] or to the film being thinner at the edges in the case of a small contact

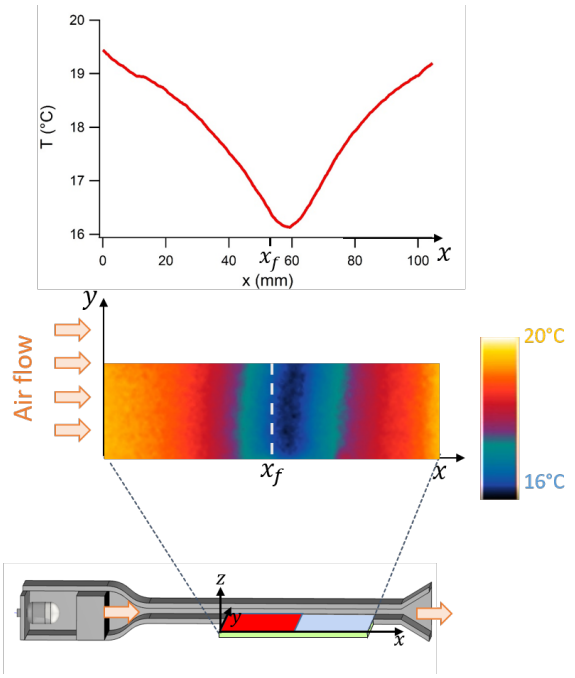

FIGURE 1 – Cut view of the wind tunnel in which the film of polymer solution spread on a glass plate is made to dry. Air is injected through a honeycomb structure and a laminar flow forms above the liquid film. The film is imaged from above with an infrared camera and through an infrared-transparent window. An example of thermal image acquired during front propagation is shown with its color scale. The above temperature profile was obtained by averaging the image along the direction of the y-axis, i.e. over 3 cm. The room temperature was 19.7°C, the average initial thickness of the film 15 µm and the air velocity 3 cm.s^{-1}.

angle[16]. The formed fronts propagate towards the center as the film dries [17]. Different techniques have been used to measure the displacements of the fronts. In colloidal suspensions, in which drying may change light scattering, the fronts can be directly visualised [4, 15]. In other systems however, the front may not be visible and more sophisticated techniques such as Small Angle X-ray Scattering (SAXS) [12] or Nuclear Magnetics Resonance (NMR) microscopy [18] have been used. In addition to the heavy instrumentation necessited, they require either that the front passage induces a change in the microstructure for SAXS, or the addition of a specially designed probe for NMR microscopy.

Herein, we provide a quantitative study of the drying fronts that form during the convective drying of films of polymer solutions based on a very simple technique. We perform temperature measurements of a drying film with an infrared camera and we demonstrate that they can be used to monitor the front position due to the cooling resulting from drying. In addition, we show that spatial variations in the drying rate can be quantitatively determined from both the temperature profiles and a thermal calibration of the system.

2 Experimental section

2.1 Wind tunnel

The experimental set-up is composed of a homemade, specially designed, wind tunnel inside which a 95mm×90mm glass plate can be inserted, as shown in Fig. 1. The glass plate is placed on a two-axis rotational stage to ensure horizontality. The wind tunnel consists of a collector at its entry, a central rectangular duct of width $W = 110$ mm and height $d = 5$ mm, and of a diffuser at its end. The design and dimensions of the wind tunnel ensure that the air flow is laminar in the central area, which is crucial for a correct description

of drying since vortices have been shown to have large effects on mass transfer [10]. The Reynolds number $\mathrm{Re} = \frac{Ud}{\nu}$, with ν the kinematic viscosity of air, is at most 60, which is well below the critical value for unstable flows [7]. The sample is placed 5 cm after the entry of the central duct, at a distance larger than that for the development of a Poiseuille flow, and at the same height as the surface of the bottom wall of the wind tunnel. More generally, sharp edges that could break laminarity have been carefully avoided. Dry air with at most 3ppm water (Air Products) is injected in the wind tunnel. The average air velocity, which is controlled with a flowmeter (SNC), ranges from 0.6 to 12 cm.s^{-1}, resulting in negligible entrainment of the liquid and well below the threshold for the onset of Kelvin-Helmholtz instabilities at the air/liquid interface [7]. We use a thermal camera (array of uncooled microbolometer, spectral range 7.5-14µm, resolution 640x480 pixels) with an objective lens of f-number 1.3 (kit camera and objective lens FLIR A700 24°). It images the plate from above, through the upper wall of the wind tunnel made of an infrared-transparent polymer film (Edmund Optics). The temperature measured by the camera accounts for the thermal emissivity, which is very close to 0.95 for glass, water and the polymer whose solution is dried in the experiments.Temperature profiles are further extracted from the thermal images by averaging the temperature over 3 cm in the y-axis direction. An example is shown in fig. 1.

2.2 Polymer solutions

The polymer solutions are aqueous maltodextrin solutions, of volume fraction 0.143 which are prepared by adding maltodextrin of dextrose equivalent 2 and molar mass $M = 343\ 000$ g.mol^{-1} (Glucidex 2, Roquette) to deionized water. The solutions are stirred at room temperature until complete dissolution before use. Maltodextrin is an amorphous polymer that undergoes a glass transition in solvent at room temperature : it becomes glassy at solvent volume fractions smaller than 0.24 for the considered molar mass [1]. Prior to drying experiments, polymer solutions are spread on clean glass plates (dimensions 95 mm × 90 mm). Wire-wound-rods of different sizes (BYK) are used to obtain liquid films of initial thicknesses h_0 ranging from 15 to 130 µm. The values of the initial thicknesses are not fully controlled with the adopted deposition process. As a result, the spatially averaged thickness of the dried layers, h_d, were systematically measured with an optical profilometer (Zygo) after each drying experiment. The values of the average initial thicknesses are inferred from both those measurements and the volume fraction of remaining solvent at the time of those measurements, whose value was determined by gravimetry to be 0.15 ± 0.05, i.e. below glass transition.

2.3 Thermal calibration

In order to characterise the temperature decrease resulting from water evaporation, calibration experiments have been performed, in which the temperature of a glass plate that is locally heated is measured. A conductive (Indium Tin Oxyde, ITO) strip of width 2 mm is primarily sputtered on a glass plate, at a distance $x_0 = 40$ mm from the edge of the plate. The plate is then placed in the wind tunnel with the ITO strip along the y-axis. An electrical power P is further injected in the stripe and the temperature of the plate is measured with the infrared camera under constant air flow. After a transient regime lasting a few minutes, stationary temperatures profiles, as shown in fig. 2, are measured. We have found that the temperature profiles are well described by

$$T = T_0 + P\alpha(U)g\left(x - x_0, U\right) \tag{1}$$

where P is the electrical power and $\alpha(U)$ a coefficient that depends on the air velocity U. T_0 is room temperature, independently measured with a thermometer. The function g accounts for the thermal exchanges with air and the glass plate, as well as in plane heat conduction. It is normalised such that its maximum value, reached for $x = x_0$, is equal to 1. Its shape is well described by an heuristic expression, which is inspired by previous measurements on a similar system [14], of the form

$$g(x) = \left(\frac{2}{e^{\beta\frac{x}{\zeta}} + e^{-\frac{x}{\zeta}} + (1-\beta)\frac{x}{\zeta}}\right)^{\frac{\zeta}{\zeta_\theta}} \tag{2}$$

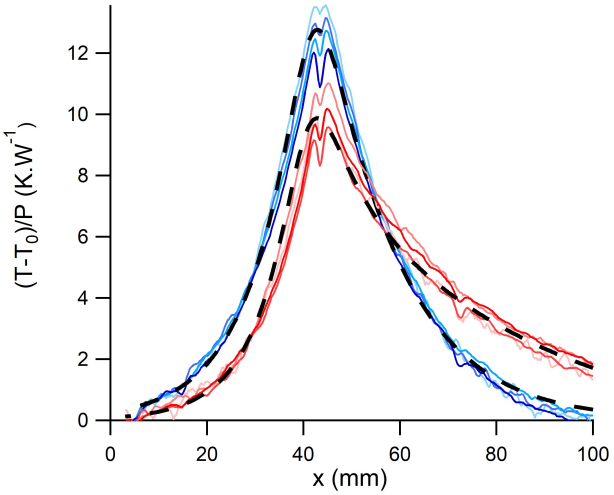

FIGURE 2 – Temperature increase normalised by the injected electrical power measured in the calibration set-up. The data obtained for electrical powers of 0.07 W, 0.13 W, 0.21 W and 0.31 W are shown with lines from lighter to darker colour, with average air velocities $U = 0.6$ cm.s^{-1} (blue) and $U = 9.1$ cm.s^{-1} (red). The hatched line is a fit to the experimental data following equation 1.

with ζ a length that accounts for the effects on temperature of the finite size of the conductive strip, $\zeta = 4$ mm whatever the air velocity. ζ_θ is the characteristic lateral length of heat propagation, both by air and by the glass plate. The parameter β is introduced to account for the asymmetry of the temperature profile resulting from heat convection by the air flow. The third term in the denominator forces the position of the maximum to $x = 0$. The dimensionless parameter β and the length ζ_θ both decrease with increasing air velocity. Their values are shown in Table 1.

TABLE 1 – Values of air velocity and corresponding values of the parameters of the calibration experiment defined in eq. 1 and 2, and of length ξ given by eq. 9

U(cm.s^{-1})	α(K.W^{-1})	β	ζ_θ(mm)	ξ (mm)
0.6	12.72	0.72	10.3	3.9
1.5	12.56	0.60	10.7	9.7
3.0	11.67	0.49	9.5	19.4
9.1	9.87	0.30	8.5	58.3
12.1	8.52	0.26	8.2	77.7

3 Results and Discussion

3.1 Temperature profiles

Temperature profiles measured in a drying film of maltodextrine solution are shown in Fig. 3. Drying is associated with a drop in temperature of up to 5 °C. Clearly, a stationary regime is reached far enough from the edges of the plate, i.e. roughly between 30 and 80 mm from the upstream edge in the example of fig. 3. This result is better observed in Fig. 4 that reports the position of the minimum of the temperature profiles as a function of time. A constant front velocity v_f can thus be defined from the temperature curves. Its value depends on both the film thickness and air velocity and ranges from a few microns to a few tens of microns per second. Interestingly, the spontaneous fronts that form during non-convective drying do not

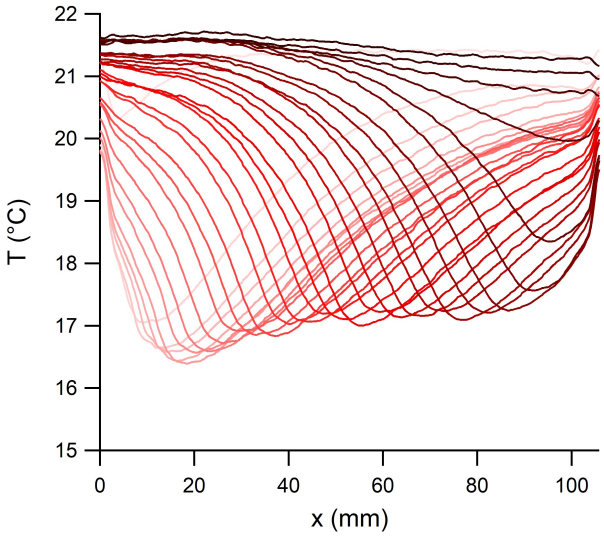

FIGURE 3 – Temperature profiles measured in a drying film. Profiles recorded every 5 minutes from the beginning of drying are shown with increasingly darker color. The profiles have been averaged in a 3 cm-wide area. The room temperature is 21.5°C, the air velocity $U = 3$ cm.s^{-1} and the film initial average thickness $h_0 = 121$ µm.

move at a constant velocity in films of rectangular shape [15]. Here, it is likely the forced uniform air flow that is responsible for the uniform motion observed.

We now show how temperature profiles can be used together with the thermal calibration to determine the local drying rate of the film. The decrease in temperature in the film results from the vaporisation of water. The part of film located between x' and $x' + dx'$ absorbs the power $-W dx' L_v \rho \dot{e}(x')$ to vaporize, where W is the dimension of the film in the y-direction, L_v the latent heat of vaporisation of water ($L_v = 2.45$ MJ.kg^{-1}), ρ its density. $\dot{e}(x')$ is the local drying rate at location x', defined as the vertical velocity of the liquid/air interface, $\dot{e} = -\frac{\partial h}{\partial t}$. The temperature variations of the film can be inferred by accounting for the thermal exchanges at stake, i.e. by convolving the absorbed power and the function g determined in the calibration experiments. It yields

$$T(x) = T_0 - \alpha W L_v \rho \int_0^L \dot{e}(x') g(x - x') dx' \tag{3}$$

In what precedes, we have assumed that the temperature decrease is instantaneous. This approximation is justified by the small response times measured in the calibrations compared to the propagation times of the drying front.

We have used eq. 3 to determine the local drying rate from the experimental temperatures profiles. For this purpose, we have assumed a given form of the drying rate, which is detailed in the following paragraph.

3.2 Drying rate

The chosen drying rate $\dot{e}(x)$ is based on the exact resolution for the drying of a semi-infinite film placed in a convective flow of a uniform shear rate in an unbounded medium [11], yielding a power law decrease of drying rate with the distance to the front, $\dot{e} \propto (x - x_f)^{-\frac{1}{3}}$. In this picture, the drying rate diverges at the front, as invoked for instance at the edges of a drying droplet as the possible cause for the "coffee-stain effect" [3].

We detail below how the concentration field is obtained. We consider a drying film placed in a horizontal air flow and we use the axes defined in Fig. 5. We assume that the air velocity close to the surface of the film is given by $U = \dot{\gamma} z$, where $\dot{\gamma}$ is the shear rate, and that the diffusion coefficient of vapor in air is D. The

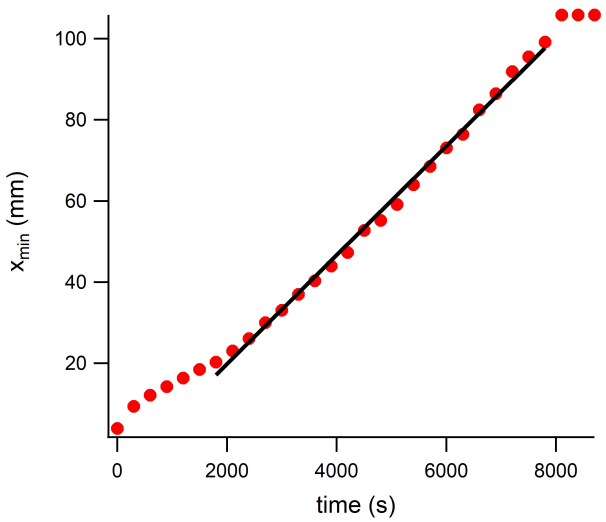

FIGURE 4 – Position of the minimum temperature as a function of time, measured from the temperature profiles of fig. 3.

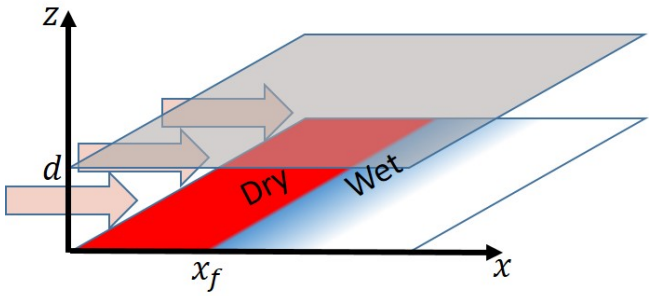

FIGURE 5 – Scheme and notations of the liquid film drying in the wind tunnel of height d. The drying front separates the dry film from the wet one.

concentration field c of vapor above the film and at position $x > x_f$, depends on the distance to the drying front $x - x_f$ and on the vertical distance to the film, i.e. $c(x - x_f, z)$, and follows the advection-diffusion equation, which, in stationary conditions, reads

$$\dot{\gamma} z \frac{\partial c}{\partial x} - D \frac{\partial^2 c}{\partial z^2} = 0 \tag{4}$$

Following a similar resolution as Levich's [11],we introduce the dimensionless quantity

$$\eta = \frac{\dot{\gamma} z^3}{9D(x - x_f)} \tag{5}$$

The concentration $c(\eta)$ verifies

$$3\eta c''(\eta) + (3\eta + 2)c'(\eta) = 0 \tag{6}$$

with the boundary conditions $c(\eta \to 0^+) = c_{sat}$, i.e. for $z = 0^+$ and $x > x_f$ and $c(\eta \to +\infty) = c_\infty$ i.e. for $z > 0$ and $x > x_f$. Equation 6 can be integrated and finally yields

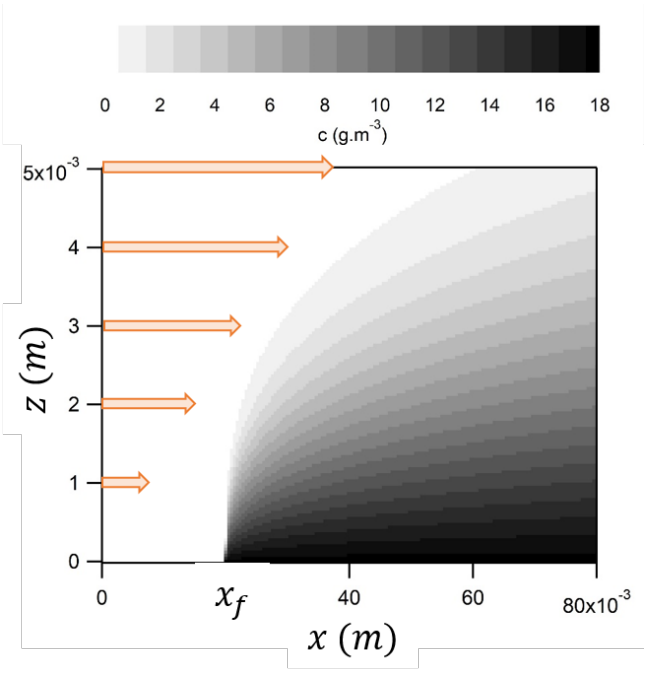

FIGURE 6 – Concentration field computed from eq. 7 with $x_f = 20$ mm, $c_\infty = 0$, $c_{sat} = 18$ g.m^{-3} and $D = 2.6 \times 10^{-5}$ m^2.s^{-1} which are values corresponding to evaporation of water by a dry air flow. The shear rate is $\dot{\gamma} = 145.2$ s^{-1}, corresponding to an air velocity of 12.1 cm.s^{-1} in the wind tunnel.

$$c(x - x_f, z) = c_{sat} + (c_\infty - c_{sat}) \frac{\int_0^{\frac{\dot{\gamma} z^3}{9D(x-x_f)}} \eta^{-\frac{2}{3}} e^{-\eta} d\eta}{\int_0^\infty \eta^{-\frac{2}{3}} e^{-\eta} d\eta} \tag{7}$$

where c_{sat} is the vapor concentration at saturation and c_∞ the vapor concentration far away from the film. The resulting concentration field for $c_\infty = 0$ is displayed in fig. 6. It is shown for a position of the drying front $x_f = 20mm$ and in a section corresponding to that of the wind tunnel. We emphasise that eq. 7 is obtained in an unbounded medium and we discuss later the differences that are expected in the bounded medium constituted by the wind tunnel.

The drying rate of the film $\dot{e} = -\frac{D}{\rho} \left(\frac{\partial c}{\partial z}\right)_{z=0}$, where ρ is the density of liquid water, is thus given by

$$\dot{e}(x - x_f) = 0.538 \left(c_{sat} - c_\infty\right) \frac{\dot{\gamma}^{\frac{1}{3}} D^{\frac{2}{3}}}{\rho} \left(x - x_f\right)^{-\frac{1}{3}} \tag{8}$$

The vapor concentration in equilibrium with a polymer solution is given by ac_{sat}, where a is the activity of the solvent, which itself varies with the solvent volume fraction in the solution. Since this variation is weak at large solvent content [5], we make the approximation that, before the passage of the front, the activity of water remains equal to that of the initial solution, i.e. $a \simeq 1$. We emphasise that, after the passage of the front, the solvent content of the film is not zero. Nevertheless, we expect that both the solvent activity and diffusion coefficient of water in the glassy layer are small [5], and this is why we make the approximation of a vanishing drying rate upstream of the front. In the following, the assumption we make of a sharp change in water activity at the front results in a diverging drying rate as that in eq. 8.

A characteristic distance ξ can be inferred from the dimensionless parameter η given by eq. 5, $\xi = \dot{\gamma} d^3/9D$. The height of the wind tunnel d is the characteristic vertical length ; U is the average velocity of the air flow along the z-axis, hence the shear rate at $z = 0$ of the Poiseuille air flow is $\dot{\gamma} = 6U/d$. The length ξ is

therefore given by

$$\xi = \frac{2Ud^2}{3D} \tag{9}$$

The values of ξ are reported in Table 1, they vary from a few millimeters to almost 80 mm. Introducing the length ξ in eq. 8, the drying rate can be expressed as

$$\dot{e} = 1.120\,(c_{sat} - c_\infty)\,\frac{D}{d\rho}\left(\frac{x - x_f}{\xi}\right)^{-1/3} \tag{10}$$

The drying rate in an unbounded medium given by eq. 10 is expected to be valid in the wind tunnel at small distances from the drying front. However, at distances from the front larger than a length we denote ξ^*, the saturation of the atmosphere across the height of the bounded tunnel modifies the drying rate. In order to deconvolve the thermal signal, we suggest the following ansatz for the evaporation rate. We take into account the decrease in the evaporation rate at distances greater than ξ^* by an exponentially decreasing rate. Imposing continuity of the drying rate and of its first derivative at the boundary between power law and exponential decrease i.e. at $x - x_f = \xi^*$, yields the following expressions of the drying rate
If $x - x_f < 0$

$$\dot{e} = 0 \tag{11}$$

If $0 < x - x_f < \xi^*$

$$\dot{e} = \dot{e}_0 \left(\frac{x - x_f}{\xi}\right)^{-\frac{1}{3}} \tag{12}$$

If $x - x_f \geq \xi^*$

$$\dot{e} = \dot{e}_0 \left(\frac{\xi}{\xi^*}\right)^{\frac{1}{3}} e^{-\frac{x - x_f + \xi}{3\xi}} \tag{13}$$

where $\dot{e}_0$ is the amplitude of the drying rate. As discussed above, the assumption we make about the drying rate on each side of the drying front is based on the highly non-linear behaviour of water activity as a function of polymer volume fraction. Consequently, we neglect the precise variations in activity close to the front, which is justified if they occur over a very small distance. In this picture, the drying rate diverges at the drying front and we emphasise that it makes direct deconvolution of the drying rate from the experimental temperature profiles using eq. 3 difficult ; this is why we have rather assumed the shape of $\dot{e}(x)$ given above.

Figure 7 shows two examples of experimental temperature profiles together with the profiles obtained by fitting eq. 3 to the experimental profiles, using a drying rate given by eq. 11, 12 and 13. The three fitting parameters are x_f, ξ^* and $\dot{e}_0$, all the other parameters being determined by the experimental conditions. A good description of the profile shapes is obtained for all air velocities and film thicknesses. The front position x_f is found to be upstream of the position of the minimum temperature. The decay length at large distances, ξ^* depends on both air velocity and film thickness. As the value of the initial film thickness differs in each experiment, due to the deposition process, it is difficult to deduce trends from the measured values of ξ^*. Nonetheless, we have found that the ratio ξ^*/ξ, decreases with increasing air velocity : it ranges from about 2 at the lowest velocity to about 0.1 at the largest velocity.

An example of drying rate is shown in fig. 8. The amplitude $\dot{e}_0$ is found to be of the same order of magnitude as that given by eq. 10, i.e. of the order of 10^{-7} m.s^{-1}, obtained with $c_\infty = 0$, $c_{sat} = 18$ g.m^{-3} and $D = 2.6 \times 10^{-5}$ m^2.s^{-1}. We further comment on the values of this fitting parameter in the following.

In summary, we demonstrate that drying rates can be quantitatively determined from temperature measurements. As a further validation, we show in the next sections that global mass balances can also be used to determine the velocity of the drying front from the drying rate, as well as the amplitude $\dot{e}_0$.

3.3 Relation between front velocity and drying rate

We now use a simple mass balance to determine the front velocity from the drying rate. Since the drying rate is related to the sample thickness h by $\frac{\partial h}{\partial t} = -\dot{e}$, integration between times $t = 0$ and $t = t_d$, where t_d

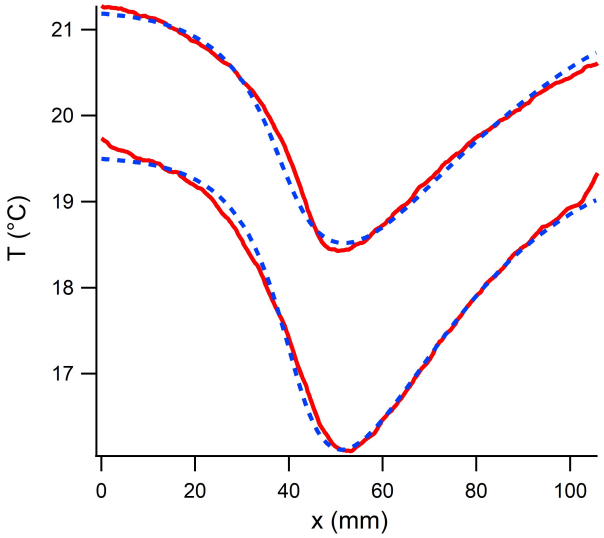

FIGURE 7 – Experimental (red lines) and fitted profiles (blue dotted lines) following eq. 3, where the drying rate is given by eq. 12 and 13 with $\dot{e}_0$, x_f and ξ^* as fitting parameters. The average air velocities and initial film thicknesses are respectively 1.5 cm.s^{-1} and 98 µm (top curve) and 3 cm.s^{-1} and 69 µm (bottom curve).

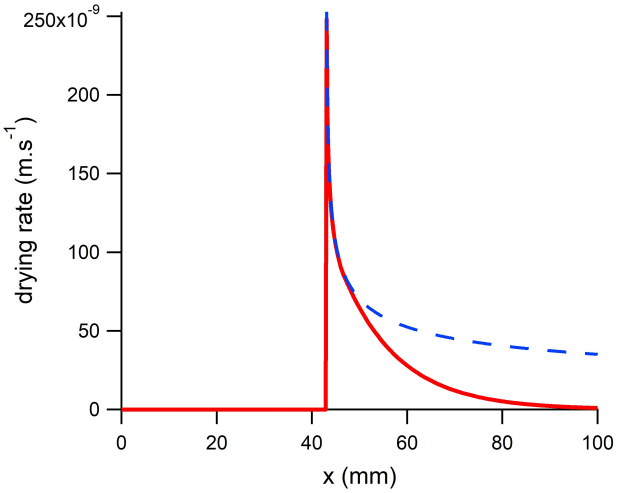

FIGURE 8 – Drying rate (red line) as a function of the distance to the edge of the film. The hatched line shows the power law decay of eq. 12 followed at small distances to the front, whereas the drying rate decreases exponentially at larger distances, following eq. 13. The parameters $\dot{e}_0 = 4.9 \times 10^{-8}$ m.s^{-1}, $x_f = 42.9$ mm and $\xi^* = 4$ mm were determined by a fit to the experimental temperature profile of fig. 7 obtained for an air velocity $U = 3$ cm.s^{-1}, while the distance $\xi = 19.4$ mm given by eq. 9 is set by the experimental conditions.

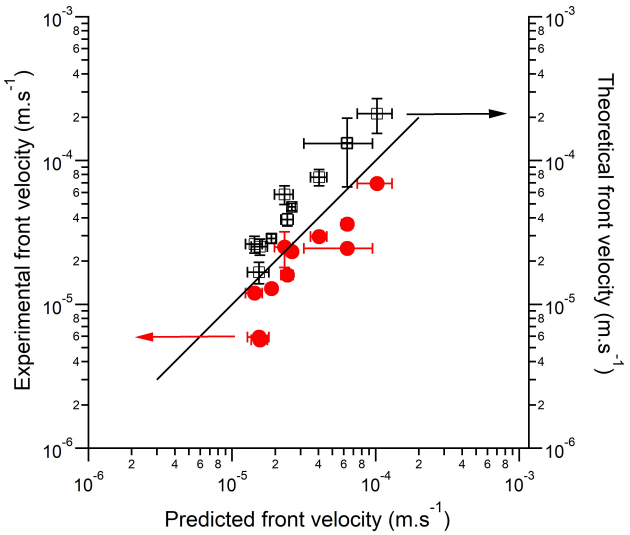

FIGURE 9 – Front velocity measured from the temperature profiles (circles/left axis) as a function of the front velocity predicted by eq. 17. The horizontal error bars result from the uncertainties on the dry and initial thicknesses of the film. The vertical error bars are too small to appear. The full line is the $y = x$ line. The front velocity given by the global balance of eq. 18 is shown as black squares (right axis).

it the total drying time, yields

$$h_0 - h_d = \int_0^{t_d} \dot{e} dt \tag{14}$$

Using that the front moves at constant velocity v_f, the integral can be turned into a space integral along the length L of the film

$$h_0 - h_d = \frac{1}{v_f} \int_0^{L} \dot{e} dx \tag{15}$$

leading to

$$v_f = \frac{\int_0^L \dot{e} dx}{h_0 - h_d} \tag{16}$$

Using the expression of the drying rate given by eq. 11, 12 and 13, after integration, the front velocity is given by

$$v_f = \frac{9\dot{e}_0 \xi^{\frac{1}{3}} \xi^{*\frac{2}{3}}}{2\,(h_0 - h_d)} \left(1 - \frac{2}{3} e^{-\frac{L - x_f - \xi^*}{3\xi^*}}\right) \tag{17}$$

Figure 9 shows the measured front velocity as a function of that predicted by eq. 17. Within the range of air velocities and film thicknesses investigated, the front velocity varies by almost one order of magnitude and a good agreement is obtained between the experimental and predicted values. Therefore, eq. 17 provides a quantitative prediction of the front velocity.

A global conservation argument can also be used to predict the front velocity. As shown above, the vaporized amount of solvent is $(h_0 - h_d)v_f$, which is a flow rate per unit of of length in the y direction. It must be equal to the flow rate of solvent vapor in the wind tunnel, i.e.

$$v_f\,(h_0 - h_d) = \frac{c_{sat} U d}{\rho} \tag{18}$$

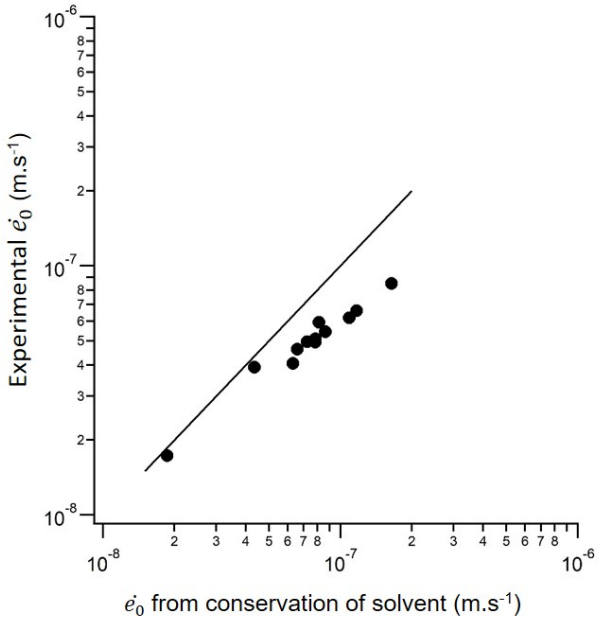

FIGURE 10 – Amplitude of the drying rate obtained by fits to the experimental temperature profiles as a function of that computed using eq. 19. In the latter equation, ξ is computed using eq. 9 and ξ^* is obtained from fits to the temperature profiles. The value of the concentration at saturation c_{sat} is that at 20° C. The full line is the $y = x$ line.

The values of the front velocity obtained by eq. 18 are shown in fig. 9. Consistently, they are close to those predicted by eq. 17, **although they systematically overestimate the front velocity.** In the next section, we further discuss this small discrepancy by analysing its consequences on the amplitude of the drying rate.

3.4 Amplitude of the drying rate

Using eq. 17 and eq. 18 the expression of the amplitude of the drying rate reads

$$\dot{e}_0 = \frac{1}{3\left(1 - \frac{2}{3}e^{-\frac{L-x_f-\xi^*}{3\xi^*}}\right)} \left(\frac{\xi}{\xi^*}\right)^{\frac{2}{3}} \frac{c_{sat}D}{\rho d} \tag{19}$$

Equation 19 is similar to the amplitude of the drying rate in an unbounded media given by eq. 10, but with an air-velocity-dependent prefactor, which involves the ratio of the lengths ξ and ξ^*. In fig. 10, we display the amplitude of the drying rate obtained by the fit of the temperature profiles as a function of those given by eq. 19. The larger experimental values of $\dot{e}_0$ deviate from those predicted by solvent conservation. We believe that this small discrepancy results from the poorer description of the drying rate singularity at the largest air velocities. At the latter values, the ratio ξ^*/ξ becomes small, as emphasised above, and the exponential decay does not well capture the variations of the drying rate. The overall good agreement between both amplitudes nevertheless shows the validity of the infrared measurements for a quantitative determination of the drying rate.

4 Conclusions

In conclusion, we have studied the propagation of drying fronts in films of polymer solutions dried in laminar air flows. We show that temperature measurements using an infrared camera provide not only a characterisation of the kinetics of the drying front, but also quantitative measurements of the spatial variations of the drying rates. Since the measurements do not require any specific properties of the sample, our results pave the way for a better characterisation of kinetics of drying of large classes of systems.

Acknowledgements : We are very grateful to Marc Fermigier for helping us to design the wind tunnel.

Références

[1] F. Avaltroni, Pierre-Etienne Bouquerand, and Valéry Normand. Maltodextrin molecular weight distribution influence on the glass transition temperature and viscosity in aqueous solutions. *Carbohydrate Polymers*, 58(3) :323–334, 2004. Publisher : Elsevier. Cité page 3

[2] Tobias Börnhorst, Philip Scharfer, and Wilhelm Schabel. Drying Kinetics from Micrometer- to Nanometer-Scale Polymer Films : A Study on Solvent Diffusion, Polymer Relaxation, and Substrate Interaction Effects. *Langmuir*, 37(19) :6022–6031, May 2021. Cité page 1

[3] Robert D. Deegan, Olgica Bakajin, Todd F. Dupont, Greb Huber, Sidney R. Nagel, and Thomas A. Witten. Capillary flow as the cause of ring stains from dried liquid drops. *Nature*, 389(6653) :827–829, October 1997. Publisher : Nature Publishing Group. Cité pages 1 et 5

[4] V. Divry, A. Gromer, M. Nassar, C. Lambour, D. Collin, and Y. Holl. Drying Mechanisms in Plasticized Latex Films : Role of Horizontal Drying Fronts. *J. Phys. Chem. B*, 120(27) :6791–6802, July 2016. Cité page 2

[5] Julien Dupas, Emilie Verneuil, Maxime Van Landeghem, Bruno Bresson, Laurent Forny, Marco Ramaioli, Francois Lequeux, and Laurence Talini. Glass Transition Accelerates the Spreading of Polar Solvents on a Soluble Polymer. *Phys. Rev. Lett.*, 112(18) :188302, May 2014. Cité page 7

[6] Lucas Goehring, William J. Clegg, and Alexander F. Routh. Solidification and Ordering during Directional Drying of a Colloidal Dispersion. *Langmuir*, 26(12) :9269–9275, June 2010. Cité page 1

[7] Etienne Guyon, Jean Pierre Hulin, Luc Petit, and Catalin D. Mitescu. *Physical Hydrodynamics*. Oxford University Press, 2015. Google-Books-ID : bi8TDAAAQBAJ. Cité page 3

[8] A. Hallajisani, S. J. Hashemi, and W. J. Murray Douglas. Experimental Investigation of Industrial Coating-Drying Process Parameters. *Drying Technology*, 29(13) :1484–1491, October 2011. Publisher : Taylor & Francis _eprint : https ://doi.org/10.1080/07373937.2011.575973. Cité page 1

[9] Kota Hatakeyama, Kanji Tanaka, Tsutomu Takahashi, Shiro Wakaki, and Alexander F. Routh. Measurement of volume fraction distribution in a drying film by imaging with a digital camera. *Colloids and Surfaces A : Physicochemical and Engineering Aspects*, 648 :129263, September 2022. Cité page 1

[10] Joachim Krenn, Susanna Baesch, Benjamin Schmidt-Hansberg, Michael Baunach, Philip Scharfer, and Wilhelm Schabel. Numerical investigation of the local mass transfer on flat plates in laminar flow. *Chemical Engineering and Processing : Process Intensification*, 50(5-6) :503–508, May 2011. Cité page 3

[11] Venjamin G. Levich. *Physicochemical hydrodynamics*. Prentice Hall international series in the physical and chemical engineering sciences. Prentice-Hall, Englewood Cliffs, NJ, 2. ed. edition, 1962. Cité pages 5 et 6

[12] Joaquim Li, Bernard Cabane, Michael Sztucki, Jérémie Gummel, and Lucas Goehring. Drying Dip-Coated Colloidal Films. *Langmuir*, 28(1) :200–208, January 2012. Cité pages 1 et 2

[13] L. Mayor and A.M. Sereno. Modelling shrinkage during convective drying of food materials : a review. *Journal of Food Engineering*, 61(3) :373–386, February 2004. Cité page 1

[14] M. Maza-Cuello, C. Frétigny, and L. Talini. Probing interfacial effects with thermocapillary flows. *Phys. Rev. Fluids*, 7(12) :124003, December 2022. Cité page 3

[15] M. Nassar, A. Gromer, F. Thalmann, P. Hébraud, and Y. Holl. Velocity of lateral drying fronts in film formation by drying of colloidal dispersions. A 2D simulation. *Journal of Colloid and Interface Science*, 511 :424–433, February 2018. Cité pages 2 et 5

[16] Alexander F Routh. Drying of thin colloidal films. *Rep. Prog. Phys.*, 76(4) :046603, April 2013. Cité page 2

[17] Alexander F. Routh and William B. Russel. Horizontal drying fronts during solvent evaporation from latex films. *AIChE Journal*, 44(9) :2088–2098, September 1998. Cité page 2

[18] J. M. Salamanca, E. Ciampi, D. A. Faux, P. M. Glover, P. J. McDonald, A. F. Routh, A. C. I. A. Peters, R. Satguru, and J. L. Keddie. Lateral Drying in Thick Films of Waterborne Colloidal Particles. *Langmuir*, 17(11) :3202–3207, May 2001. Cité page 2

[19] R. Saure, G.R. Wagner, and E.-U. Schlünder. Drying of solvent-borne polymeric coatings : II. Experimental results using FTIR spectroscopy. *Surface and Coatings Technology*, 99(3) :257–265, February 1998. Cité page 1

[20] B. Schmidt-Hansberg, M. F. G. Klein, K. Peters, F. Buss, J. Pfeifer, S. Walheim, A. Colsmann, U. Lemmer, P. Scharfer, and W. Schabel. *In situ* monitoring the drying kinetics of knife coated polymer-fullerene films for organic solar cells. *Journal of Applied Physics*, 106(12) :124501, December 2009. Cité page 1

[21] Simon Ternes, Tobias Börnhorst, Jonas A. Schwenzer, Ihteaz M. Hossain, Tobias Abzieher, Waldemar Mehlmann, Uli Lemmer, Philip Scharfer, Wilhelm Schabel, Bryce S. Richards, and Ulrich W. Paetzold. Drying Dynamics of Solution-Processed Perovskite Thin-Film Photovoltaics : In Situ Characterization, Modeling, and Process Control. *Advanced Energy Materials*, 9(39) :1901581, October 2019. Cité page 1